

Article

Not peer-reviewed version

A Novel Multi-Needle-to-Cylinder Dielectric Barrier Discharge Reactor with Deflector Rings for Energy-Efficient Removal of Sulfides and Ammonia from Odor Gases

[Qi Qiu](#)*, Zhuojun Zhang, Qianbing Xu, Yu Zhang, [Wuhua Li](#), [Xiangning He](#)

Posted Date: 26 December 2025

doi: 10.20944/preprints202512.2395.v1

Keywords: non-thermal plasma; multi-needle-to-cylinder reactor; odor abatement; flow field modulation; deflector ring; discharge-flow coordination



Preprints.org is a free multidisciplinary platform providing preprint service that is dedicated to making early versions of research outputs permanently available and citable. Preprints posted at Preprints.org appear in Web of Science, Crossref, Google Scholar, Scilit, Europe PMC.

Copyright: This open access article is published under a [Creative Commons CC BY 4.0 license](#), which permit the free download, distribution, and reuse, provided that the author and preprint are cited in any reuse.

Disclaimer/Publisher's Note: The statements, opinions, and data contained in all publications are solely those of the individual author(s) and contributor(s) and not of MDPI and/or the editor(s). MDPI and/or the editor(s) disclaim responsibility for any injury to people or property resulting from any ideas, methods, instructions, or products referred to in the content.

Article

A Novel Multi-Needle-to-Cylinder Dielectric Barrier Discharge Reactor with Deflector Rings for Energy-Efficient Removal of Sulfides and Ammonia from Odor Gases

Qi Qiu ^{1,2,*}, Zhuojun Zhang ³, Qianbing Xu ², Yu Zhang ², Wuhua Li ¹ and Xiangning He ¹

¹ College of Electrical Engineering, Zhejiang University, Hangzhou 310027, China

² College of Engineering, Hangzhou City University, Hangzhou 310015, China

³ College of Environmental and Resource Sciences, Zhejiang University, Hangzhou 310027, China

* Correspondence: qiuq@hzcu.edu.cn;

Abstract

Non-thermal plasma is a promising technology for odor abatement from agricultural and domestic waste. However, its widespread application is often limited by the inherent trade-off between energy efficiency and processing capacity in conventional reactors. To address this challenge, we propose a novel multi-needle-to-cylinder dielectric barrier discharge reactor integrated with a deflector ring. By synergistically optimizing the electrode topology and modulating the flow field, this reactor achieves enhanced removal of complex ammonia–sulfur odor mixtures. The underlying mechanisms were elucidated through computational fluid dynamics (CFD) simulations coupled with systematic performance evaluation. Experimental results demonstrate that an 8-needle electrode configuration provides the optimal balance between discharge density and energy efficiency. CFD simulations further reveal that the deflector ring effectively suppresses gas bypass and promotes recirculation vortices downstream, thereby extending the residence time significantly. Mechanistic studies indicate that the removal of recalcitrant inorganic sulfides (e.g., CS₂ and H₂S) follows a synergistic mass-transfer–reaction controlled process, which is markedly improved by flow field optimization. In contrast, organic sulfides are governed primarily by chemical kinetics and show little dependence on flow variations. Under an extremely short residence time of 0.57 s (corresponding to a flow rate of 2.0 m³/h) and an ultra-low specific energy input of 6.26 J/L, the system achieved nearly complete removal of organic sulfides. Even for challenging inorganic sulfides, removal efficiencies reached 80.9% for H₂S and 45.3% for CS₂, with negligible byproduct formation. By effectively coordinating discharge characteristics with flow dynamics, this study provides both theoretical insight and technical support for the development of next-generation, energy-efficient, high-throughput industrial odor control systems.

Keywords: non-thermal plasma; multi-needle-to-cylinder reactor; odor abatement; flow field modulation; deflector ring; discharge-flow coordination

1. Introduction

Odor control in agricultural and domestic waste management has become a pressing environmental issue [1]. Beyond causing severe olfactory discomfort, such emissions intensify public resistance through the “Not In My Backyard” (NIMBY) effect and undercut the prospects for sustainable industry growth [2,3]. The gas streams typically contain a complex mix of ammonia [4], sulfides that cause strong olfactory detectable even at low concentrations [5], hazardous benzene series [6], and terpenes [7]. Among these, ammonia and sulfides are the most frequent pollutants, with concentrations ranging from tens of ppb to hundreds of ppm [8], making their removal a

priority. While conventional methods like biofiltration [9] and chemical scrubbing [10] are common, they suffer from large footprints, slow responses to load fluctuations, and low efficiency with high-throughput streams. Consequently, there is an urgent industrial demand for compact, agile, and energy-efficient alternatives.

Non-thermal plasma (NTP) technology stands out for its rapid reaction kinetics and compact design [11], making it ideal for treating high-volume, low-concentration volatile organic compounds (VOCs) [12]. However, a persistent trade-off limits its wider application: the conflict between energy efficiency and gas throughput. Unlike general VOC abatement, effective odor control requires near-total removal efficiency, which invariably demands high energy consumption [13]. For example, while wire-plate pulse corona plasma can remove 93.1% of ethyl mercaptan and 100% of ammonia, it requires a specific energy input (SEI) of 65.1 J/L [14]. Similarly, double dielectric barrier discharge (DBD) systems may achieve high removal rates for carbon disulfide (86.32%–100%) but often operate at an excessive SEI of 960–3222 J/L [15]. Developing plasma technologies that balance high efficiency with low energy consumption remains a pressing goal.

Optimizing reactor geometry is a proven pathway to enhance performance. Specific electrode topologies, such as multi-needle-to-plate [16] or coaxial arrays [17], can stabilize discharges at lower voltages to save energy. Furthermore, modulating the internal flow field—for instance, through flow-field induced surface DBD [18]—can significantly improve treatment efficacy. We propose that synergistically combining electrode topology with flow field modulation is the key to efficient, low-energy pollutant removal. Our design strategy focuses on creating inhomogeneous electric fields using multi-needle arrays to induce dense micro-discharges, while actively reconstructing the gas flow path. This forces pollutants into active discharge zones, minimizing the bypass effect.

Here, we introduce a novel Multi-Needle-to-Cylinder DBD reactor equipped with Flow Deflector Rings (DR-MCDBD). This design integrates a multi-needle array to maximize micro-discharge density and uses diversion rings to mechanically redirect the flow, enhancing gas-plasma interaction. This study aims to: (1) systematically optimize the electrode configuration and discharge characteristics for high-flow conditions; (2) evaluate the system's removal performance and energy efficiency for complex sulfide-ammonia mixtures; and (3) elucidate how diversion rings enhance the degradation of different pollutants by combining Computational Fluid Dynamics (CFD) simulations with reaction kinetics. Ultimately, this work seeks to provide a theoretical foundation and technical route for the next generation of industrial odor control reactors.

2. Materials and Methods

2.1. Experimental System

The experimental system primarily consisted of a gas supply unit (air and target gas blending), a custom-made low-temperature plasma reactor, a high-frequency high-voltage AC power supply, and a gas detection and analysis system, as shown in Figure 1a. The total gas flow rate was controlled at 1, 1.5, and 2 m³/h, respectively. Air was used as the carrier gas, and the target pollutants from gas cylinders were diluted to the following concentrations: 5 ppm H₂S, 2.5 ppm CH₃SH, 10 ppm DMS, 1.25 ppm CS₂, 2.5 ppm DMDS, and 30 ppm NH₃.

The DR-MCDBD reactor was employed for the removal of these malodorous gases. The peak-to-peak voltage ranged from 7 kV to 9 kV with a discharge frequency of 20 kHz. The voltage was regulated by a single-phase AC voltage regulator (TDGC, China) and measured using an oscilloscope (MDO3024, China). Discharge images were captured using a digital camera (Sony ILCE-7M4, Japan), and the reactor's temperature distribution was monitored using a handheld infrared thermal imager (InfiRay M620, China).

The discharge power was determined using the Q-V Lissajous figure method. The SEI and Energy Efficiency (EE) were calculated using Equations (1) and (2) [19,20], where P denotes power, Q is the gas flow rate, η_i is the removal efficiency, $C_{inlet,i}$ is the inlet concentration, and M_i is the molecular weight of the pollutant. The coefficient 3.6 represents the conversion factor between Joules and kilowatt-hours.

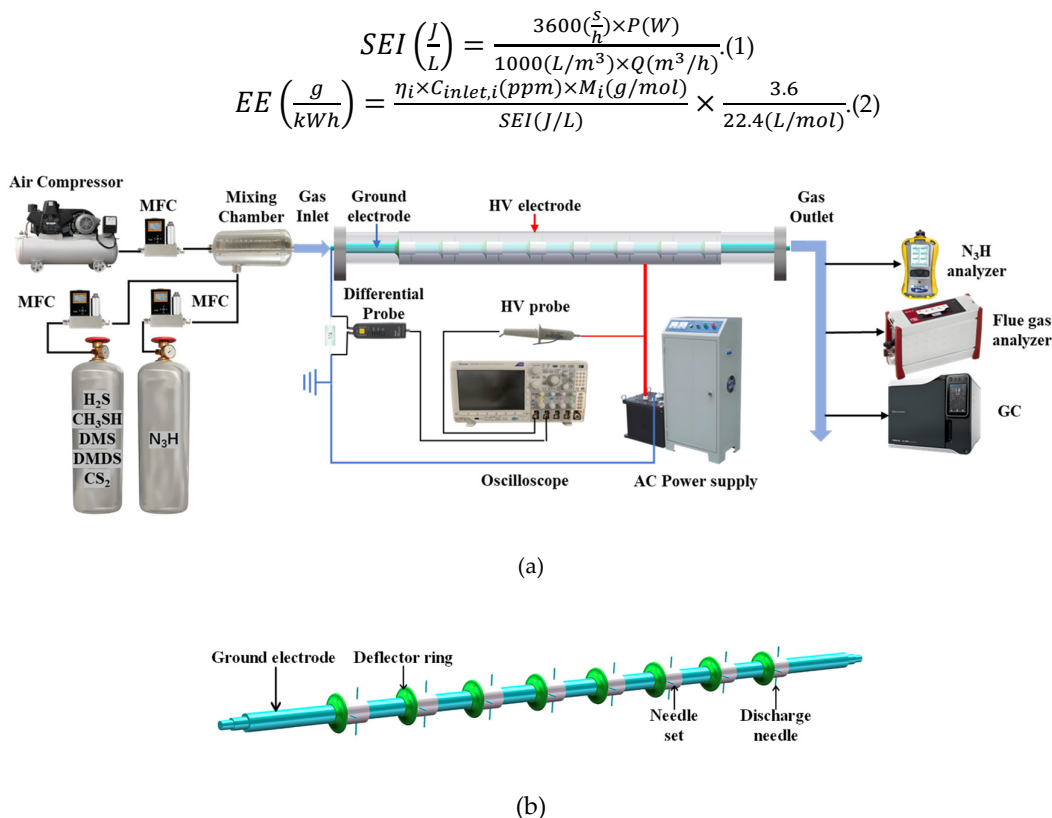


Figure 1. Schematic diagram of the experimental setup(a), DR-MC Ground electrode(b).

2.2. Reactor Configuration

To address the requirements for treating high-flow, low-concentration malodorous gases, this study designed and constructed an innovative DR-MCDBD reactor based on traditional dielectric barrier discharge (DBD) technology. The reactor aims to achieve high removal efficiency with low energy consumption by optimizing the geometric ratio between the discharge gap and the gas channel, as well as by regulating the internal flow field distribution.

The reactor features a single-dielectric coaxial configuration, comprising a quartz glass barrier tube, an external mesh high-voltage electrode, and an internal grounded electrode. A quartz tube (40 mm O.D., 3 mm wall thickness, 552 mm length) was selected as the dielectric barrier. The high-voltage electrode consists of 500-mesh 304 stainless steel mesh wrapped tightly around the outer wall of the quartz tube, with an effective discharge length of 400 mm. This dense mesh structure ensures discharge uniformity and facilitates real-time observation of the plasma state.

The internal electrode (grounded electrode) is primarily a 12 mm diameter aluminum rod, along which multiple groups (6, 8, or 10 groups) of discharge pin assemblies are arranged axially. Each assembly comprises a silicone fixing sleeve (12 mm I.D., 20 mm length, 2 mm thickness) and four 304 stainless steel discharge pins (1 mm diameter, 10 mm length). The discharge pins are distributed in pairs (180° symmetry), with adjacent pin groups staggered orthogonally (90° offset), as shown in Figure 1b. This design creates a wide annular gas channel (11 mm width) between the inner electrode and the dielectric barrier, effectively reducing flow resistance; at a flow rate of 2.0 m³/h, the gas residence time is approximately 0.57 s. Simultaneously, a 1 mm micro-discharge gap is formed between the pin tips and the inner wall of the quartz tube, providing the physical basis for inducing stable fast-pulse micro-discharges at relatively lower voltages. Furthermore, to optimize the flow field distribution within the tube, a PLA flow deflector ring (5 mm base thickness, 26 mm diameter) is installed on the upstream side of each pin assembly.

2.3. Analytical System

The inlet and outlet concentrations of sulfides were determined using a gas pre-concentrator (Acrichi APC-9LN, China) coupled with a gas chromatograph (Shimadzu Nexis GC-2030, Japan) equipped with a Flame Photometric Detector (FPD). The FPD utilized an SH-1 capillary column (60 m × 0.32 mm × 3 μm) [21]. Ammonia concentrations were measured using a portable multi-gas detector (MultiRAE PGM-82×8, USA) [22]. Ozone concentration was monitored using a handheld ozone detector (Aeroqual Series 200, New Zealand) [23], while nitrogen oxides (NO_x) and sulfur dioxide (SO₂) were analyzed using a portable infrared flue gas analyzer (MGA6 plus, Germany). Additionally, to evaluate the thermal characteristics of the reaction system, a high-precision infrared thermal imager (InfiRay M620, China) was used to monitor the thermal stability and surface temperature distribution of the reactor in real-time. The removal efficiency (η_i) for sulfides and ammonia was calculated according to Equation (3), where $C_{inlet,i}$ and $C_{outlet,i}$ represent the inlet and outlet concentrations, respectively.

$$\eta_i = \frac{C_{inlet,i}(ppm) - C_{outlet,i}(ppm)}{C_{inlet,i}(ppm)} \times 100\%.(3)$$

2.4. Numerical Simulation Setup

To elucidate the effect of the flow Deflector Ring (DR) on the flow field distribution and gas-solid/gas-liquid contact characteristics, Computational Fluid Dynamics (CFD) simulations were conducted using ANSYS Fluent. A three-dimensional (3D) computational domain was established based on the actual geometry of the multi-needle DBD reactor.

The gas flow within the reactor was assumed to be steady, incompressible, and turbulent. The SST k- ω turbulence model was employed to resolve the flow characteristics, given its robustness in predicting rotating and recirculating flows. The working fluid was set as air with standard physical properties at room temperature (25°C).

Regarding boundary conditions, a mass flow inlet was applied at the reactor entrance, corresponding to the experimental flow rate of 2 m³/h. A pressure-outlet boundary condition was set at the exit (0 Pa gauge pressure). The standard no-slip condition was applied to all wall surfaces. The second-order upwind scheme was utilized for the spatial discretization of momentum and turbulent kinetic energy to ensure calculation accuracy.

Based on a grid independence test, a mesh size of 1,070,886 cells was adopted as the standard configuration for all subsequent simulations.

3. Results and Discussion

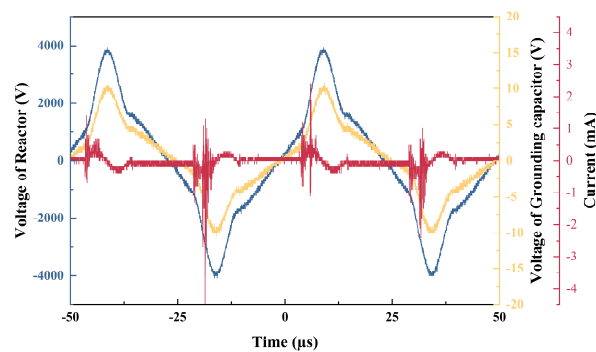
3.1. Discharge Characteristics

3.1.1. Discharge Morphology and Electrical Waveforms

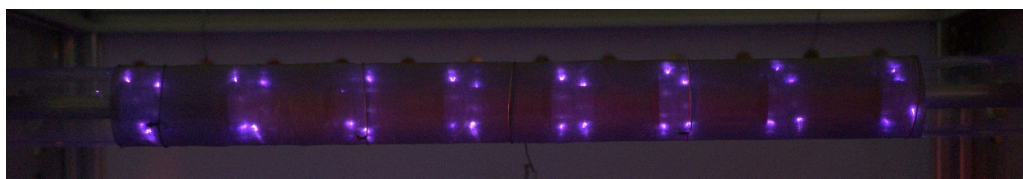
As illustrated in Figure 2a,b, the discharge within the reactor exhibits significant spatial inhomogeneity. Influenced by the microscopic radius of curvature at the needle tips, the intense electric field is highly confined to the vicinity of the needle electrodes. Consequently, the plasma is composed primarily of dense luminous spots anchored at the needle tips, while no macroscopic discharge is observed on the inner electrode surface. These luminous spots are essentially numerous discrete discharge filaments, manifesting a corona-like glow morphology macroscopically.

This physical characteristic is further corroborated by the electrical waveforms. Since the power supply operates in Discontinuous Conduction Mode (DCM) with inductive compensation, both the applied voltage and the displacement current deviate from standard sinusoidal forms [24]. Superimposed on the current waveform are dense discharge pulses, confirming that the reactor operates in a typical filamentary discharge mode. Notably, the current exhibits a significant polarity effect: the pulses are higher in amplitude and density during the negative half-cycle. This asymmetry aligns well with the characteristics of Trichel pulses, indicating that electron avalanches and space

charge accumulation near the cathode (needle tips) are more vigorous during the negative half-cycle, thereby inducing a stronger corona-type DBD.



(a)



(b)

Figure 2. Discharge characteristics of the DR-MCDBD reactor at an applied voltage of 8.0 kV. (a) Electrical waveforms of the applied voltage and current, (b) Macroscopic discharge image showing filamentary glow.

3.1.2. Power Consumption Characteristics

Figure 3a illustrates the interactive effects of the number of needle electrode sets (6, 8, and 10 sets) and the applied voltage on the discharge power. Generally, the discharge power exhibits a significant non-linear positive correlation with the applied voltage. As the voltage increases from 7.0 to 9.0 kV, the intensification of the inter-electrode electric field enhances both the frequency and intensity of micro-discharges, thereby improving the energy injection efficiency.

At a fixed voltage level, a distinct step-wise increase in discharge power is observed with an increasing number of needle sets. Specifically, at the peak voltage of 9.0 kV, the power consumption for the 6, 8, and 10-needle configurations reaches 2.9 W, 3.9 W, and 5.1 W, respectively. This enhancement is primarily attributed to the increase in effective discharge sites, which induces a greater number of discharge channels, thereby elevating the total transport current and power deposition. Notably, the power curves exhibit a distinct inflection point in the 7.5-8.0 kV range, where the growth slope is maximized. This surge signifies the reactor's transition from an initial localized corona to a fully developed filamentary discharge regime. As the voltage rises further (8.0-9.0 kV), the discharge power demonstrates a steady quasi-linear increase. In this region, the gas gap is in a stable breakdown state, the linear dependence of power on voltage observed here aligns well with the classical theory of ozonator discharge proposed by Manley [25]. This indicates that the power enhancement is governed by the theoretical scaling law, driven primarily by the increase in transferred charge per discharge cycle rather than an explosive expansion of the discharge area.

Figure 3b further investigates the influence of gas flow rate (0.5-2.5 m³/h) on the discharge power of the 8-needle reactor. The results indicate that the applied voltage is the dominant governing factor for power consumption, while the effect of gas flow rate is negligible. Even with a five-fold increase in flow rate, the discharge power remains relatively constant at a fixed voltage (e.g., 8.0 kV), showing only marginal fluctuations. This is because the development of micro-discharges occurs on the nanosecond (ns) scale, which is orders of magnitude faster than the millisecond (ms) scale residence

time of the gas flow. Consequently, aerodynamic disturbances are insufficient to alter the charge accumulation and breakdown mechanisms within the discharge gap. This flow-independent characteristic demonstrates the engineering robustness of the system, providing strong support for subsequent high-flow industrial applications.

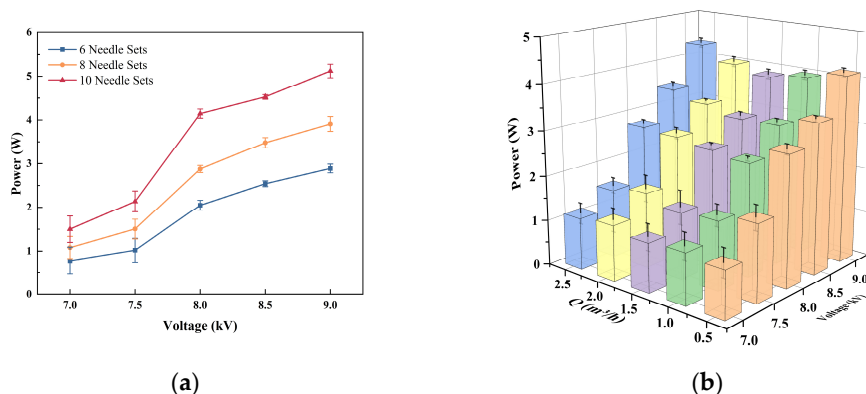


Figure 3. Discharge power characteristics of the DR-MCDBD reactor. (a) Influence of applied voltage and the number of needle electrode sets on discharge power ($1\text{m}^3/\text{h}$), (b) Combined effect of gas flow rate and applied voltage on power consumption (8-needle set configuration).

3.2. Optimization of Electrode Configuration

To determine the optimal reactor configuration capable of sustaining high-throughput conditions, the degradation characteristics were systematically evaluated under arrangements of 6, 8, and 10 needle sets. Initially, the flow rate adaptability of the 6- and 8-set arrays was examined within the range of $1.0\text{-}2.0\text{ m}^3/\text{h}$ (Figures 4 and 5). The results indicate that the 6-set configuration exhibits pronounced sensitivity to flow rate variations. As the flow rate increased, the removal efficiency of inorganic sulfides decayed significantly without exhibiting a stable plateau: the removal rates for H_2S and CS_2 plummeted from peaks of 82.4% and 57.2% to 39.5% and 38.9%, respectively. Conversely, the decline for organic sulfides was minimal ($< 2\%$).

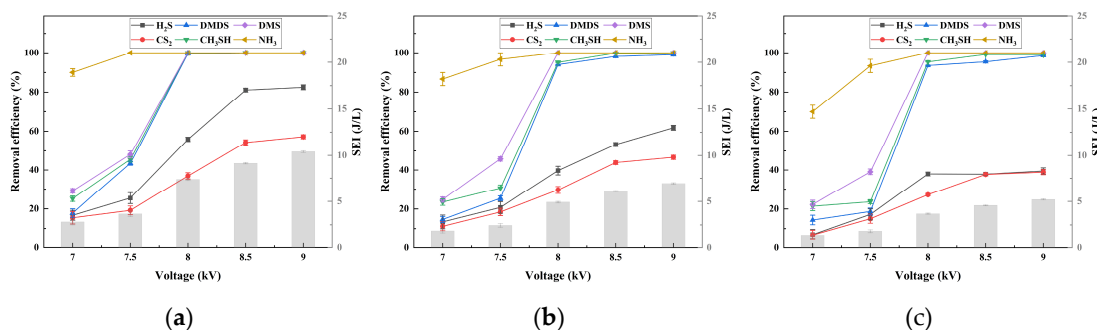


Figure 4. Decomposition characteristics of ammonia and various sulfides in the 6-needle DR-MCDBD reactor under different gas flow rates: (a) $1.0\text{ m}^3/\text{h}$; (b) $1.5\text{ m}^3/\text{h}$; and (c) $2.0\text{ m}^3/\text{h}$.

This discrepancy is attributed to the differences in degradation kinetics between the pollutants. For inorganic sulfides, the inherently sparse discharge distribution of the 6-set configuration failed to provide sufficient contact time for active species under high gas velocities (shortened residence time). In contrast, organic sulfides exhibit much faster reaction rates due to their rapid oxidation mechanisms, rendering them less sensitive to variations in residence time. Detailed reaction pathways and kinetic mechanisms for these species will be thoroughly discussed in Section 3.7.

Comparatively, the 8-set array demonstrated superior flow rate adaptability (Figure 5). Although the overall removal rate of CS_2 decreased (from 68.2% to 48.2%, a drop of approximately

20 percentage points), the efficiency stabilized within the industrially relevant range of 1.5-2.0 m³/h, with the decline controlled within 6%, forming a distinct “performance plateau.” Meanwhile, H₂S maintained a high removal level (86.0% to 81.6%). This confirms that the denser discharge network effectively increased the density of the active zone, compensating for the limitations imposed by the shortened residence time at high flow rates.

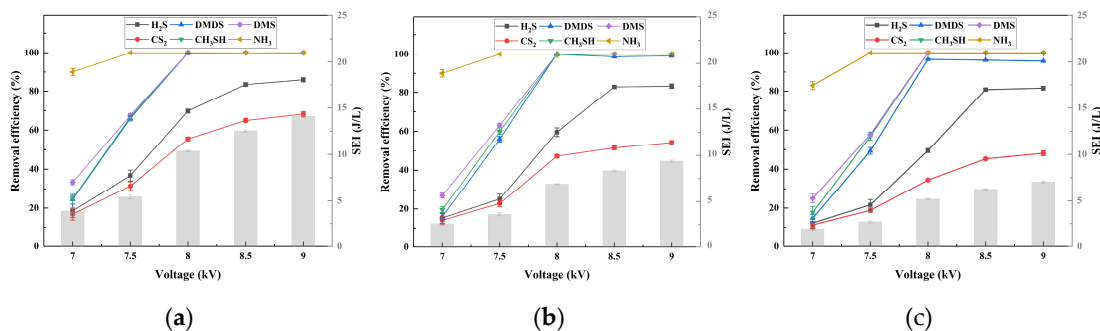


Figure 5. Decomposition characteristics of ammonia and various sulfides in the 8-needle DR-MCDBD reactor under different gas flow rates: (a) 1.0 m³/h; (b) 1.5 m³/h; and (c) 2.0 m³/h.

To further optimize the electrode configuration, a lateral comparison was conducted under typical conditions of 2.0 m³/h flow rate and 8.5 kV voltage (Note: 9.0 kV was excluded as it yielded < 4% efficiency gain but > 13% increase in SEI) (Figure 6). Increasing the number of needle sets from 6 to 8 resulted in a substantial qualitative leap in system performance, with H₂S removal soaring from 37.9% to 80.9%. This significant improvement is ascribed to the effective expansion of the active plasma volume, which drastically increased the collision probability between pollutant molecules and high-energy electrons. However, a further increase to 10 sets yielded only marginal gains (< 3% improvement for all pollutants), exhibiting a phenomenon of “diminishing marginal returns.” Since the input power increased correspondingly with the electrode number, this saturation trend is likely attributed to kinetic limitations rather than discharge suppression. As the gas passes through the first 8 sets, the pollutant concentration is significantly depleted. Consequently, in the downstream region (sets 9–10), the collision probability between active species and residual pollutant molecules decreases drastically, a factor further exacerbated by the limited residence time at high flow rates. Instead of oxidizing the pollutants, the excess active species generated by the additional power are more prone to self-recombination or quenching, leading to a decrease in energy efficiency. Consequently, the 8-set configuration, which strikes a balance between high-flow processing capacity and energy efficiency (SEI maintained at 1.94–7.04 J/L), was designated as the optimal design for this system.

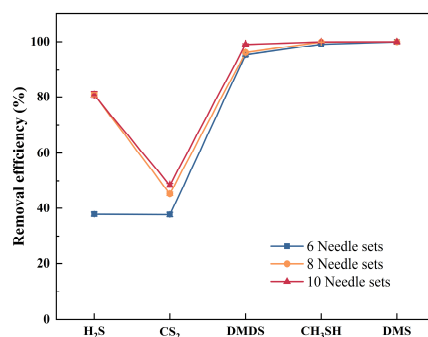


Figure 6. Comparison of pollutant removal efficiencies among different electrode configurations (6, 8, and 10 needle sets) under typical operating conditions (gas flow rate: 2.0 m³/h; applied voltage: 8.5 kV).

3.3. Energy Efficiency Analysis

The energy efficiency (EE, g/kWh) of the optimized 8-group needle configuration was characterized under varying voltages and flow rates (Figure 7). Across all flow rates, EE for ammonia and sulfides exhibited a non-monotonic trend, consistently peaking at 7.5 kV. Below this threshold, discharge intensity was insufficient for rapid degradation. Conversely, voltages exceeding 7.5 kV caused a sharp EE decline (e.g., NH₃ EE dropped from ~35 to ~12 g/kWh at 9.0 kV). This drop occurs because power consumption rises quadratically while removal rates exhibit diminishing returns, identifying 7.5 kV as the point of maximum energy economy.

Additionally, higher flow rates progressively enhanced EE, with peak NH₃ efficiency rising from ~19 to ~35 g/kWh. This is attributed to improved active species utilization; low flow rates result in excessive residence time, leading to non-productive quenching or byproduct over-oxidation. In contrast, higher flows ensure pollutant molecules effectively capture the generated plasma energy.

Regarding pollutant specificity, NH₃ and DMS achieved significantly higher EE (>30 and >20 g/kWh) compared to inorganic sulfides (<5 g/kWh). This aligns with the lower bond dissociation energies and faster reaction pathways of amino and methyl groups compared to recalcitrant inorganic structures.

Ultimately, parameter selection requires balancing economy and efficacy. Although 7.5 kV offers peak energy efficiency, removal efficiency continued to rise significantly up to 8.5 kV. Prioritizing regulatory discharge standards, 8.5 kV is recommended as the optimal operating voltage to ensure robust pollutant abatement with acceptable energy consumption.

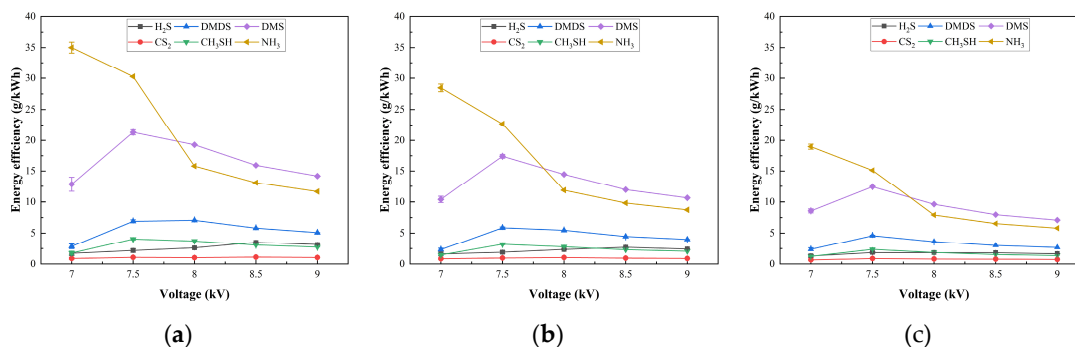


Figure 7. Energy efficiency of five typical odorous gases (NH₃ and sulfides) as a function of applied voltage under the 8-group needle configuration. (a) 1.0 m³/h; (b) 1.5 m³/h; and (c) 2.0 m³/h.

3.4. Effect of Flow Deflector Ring (DR)

3.4.1. Hydrodynamic Simulation Analysis

Figure 8a illustrates the axial velocity distribution of the cold flow field without the Deflector Ring (DR) at a flow rate of 2 m³/h. The flow field exhibits a relatively smooth distribution of streamlines. Due to the cross-sectional constriction caused by the 2-mm-thick needle holder, the maximum axial velocity reaches 1.19 m/s near the needle tips, which is approximately 1.7 times the inlet velocity. However, a low-velocity bypass region is observed near the root of the discharge needles and the inner electrode surface. Fluid passing through this region fails to penetrate the core discharge zone, potentially limiting the interaction between the gas and active species.

The flow field with the inclusion of the DR is presented in Figure 8b. The DR significantly accelerates the flow, with the maximum axial velocity peaking at 2.28 m/s at the throat of the guide plate (3.26 times the inlet velocity). The DR modifies the hydrodynamics in two beneficial ways: First, the gas forms a high-speed flow layer downstream of the throat. Given that the intense electric field is primarily concentrated near the tips of the discharge needles, this flow pattern forces the gas to traverse the region enriched with high-energy electrons and active radicals (e.g., ·OH), thereby enhancing the gas-species interaction. Second, a distinct recirculation zone is formed downstream of

the DR and the holder, with a maximum negative axial velocity of 0.8 m/s. This vortex structure promotes turbulent mixing and extends the residence time of the gas within the discharge region, further contributing to the degradation efficiency.

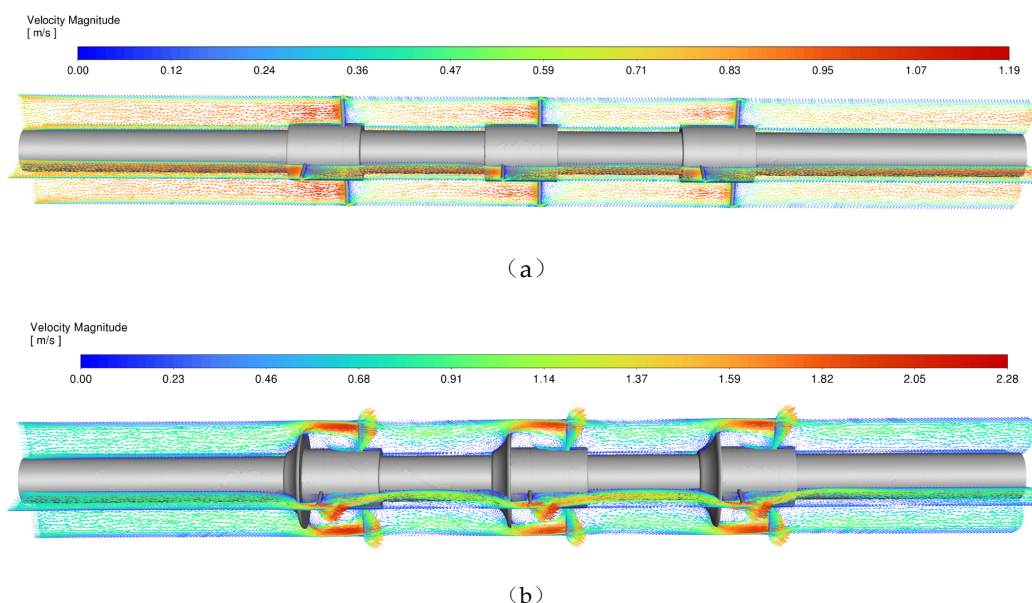


Figure 8. CFD simulation of gas velocity vector distributions at 2 m³/h: (a) Without DR, showing bypass flow; (b) With DR, highlighting flow convergence and downstream recirculation vortices.

3.4.2. Enhancement of Degradation Efficiency

To validate the theoretical benefits of the modified flow field observed in the CFD simulation, comparative experiments were conducted. Figure 9a,b present a comparative analysis of the removal efficiencies for inorganic sulfides (H₂S, CS₂) and organic sulfides (DMS, DMDS, CH₃SH) under a 6-needle electrode configuration at a flow rate of 1.5 m³/h, with and without the implementation of a Deflector Ring (DR).

As shown in Figure 10a, the introduction of the DR resulted in a pronounced enhancement in the degradation of inorganic species. For H₂S, the removal efficiency with the DR (H₂S-DR) increased linearly with voltage, reaching approximately 62% at 9.0 kV, significantly outperforming the configuration without the DR (~36%). A similar, albeit slightly less dramatic, improvement was observed for CS₂, where the DR increased removal efficiency by roughly 10–15 percentage points across the voltage range. This substantial divergence indicates that the degradation of these inorganic species is highly sensitive to hydrodynamic conditions, hinting at a mass-transfer limitation in the absence of the DR.

In stark contrast, Figure 10b reveals a negligible impact of the DR on the removal of organic sulfides. Both the DR-equipped and non-DR configurations exhibited nearly identical performance curves. The removal efficiencies for DMDS, DMS, and CH₃SH surged sharply between 7.0 and 8.0 kV, achieving near 100% removal at voltages above 8.0 kV regardless of the presence of the DR.

This overlap suggests that the removal of organic sulfides is primarily governed by energy input (voltage) rather than gas flow patterns, characteristic of a kinetic-controlled regime. Further analysis regarding the underlying reaction mechanisms and bond dissociation energies will be discussed in Section 3.7.

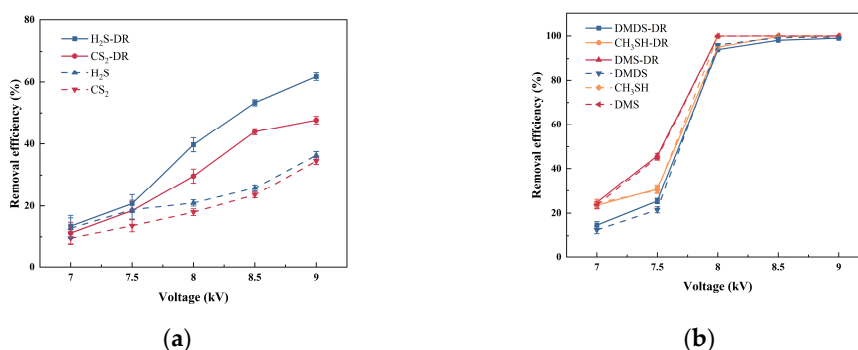


Figure 9. Comparison of removal efficiencies with and without the Deflector Ring (DR) under a 6-needle electrode configuration at a flow rate of 1.5 m³/h: (a) Inorganic sulfides; (b) Organic sulfides.

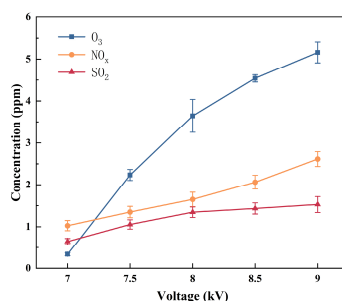


Figure 10. Effect of applied voltage on by-product generation in the 8-needle reactor at 2 m³/h.

3.5. By-Product Analysis

Figure 10 illustrates the variations in the concentrations of secondary pollutants (O₃, NO_x, and SO₂) with applied voltage (7.0–9.0 kV) in the optimized 8-needle reactor at a flow rate of 2 m³/h. The results indicate a monotonic increase in the generation of all three by-products as the discharge voltage rises. Specifically, ozone (O₃) concentration exhibited the most significant growth, rising sharply from less than 0.5 ppm at 7.0 kV to approximately 5.2 ppm at 9.0 kV. This is primarily attributed to the enhanced electric field strength at higher voltages, which intensifies the electron-impact dissociation of oxygen molecules in the background gas ($O_2 + e^- \rightarrow 2O \cdot$), thereby promoting ozone synthesis. Concurrently, NO_x concentration increased linearly, reaching about 2.6 ppm at 9.0 kV. This increase is linked to the enhanced oxidation of nitrogen species, originating from both the background air and the decomposition of ammonia. In contrast, SO₂ generation remained at a low level (<1.5 ppm) with a moderate growth trend, likely originating from the oxidation of sulfur-containing intermediates. Notably, at the recommended operating voltage of 8.5 kV, the ozone concentration was maintained below 4.6 ppm. This suggests that while increasing voltage enhances active species density, it also heightens the risk of secondary pollution.

3.6. Performance Comparison with Other Studies

Table 1 benchmarks the DR-MCDBD reactor against representative NTP systems reported in recent literature. Conventional technologies (e.g., DBD, corona, and gliding arc) typically face a trade-off between performance and energy, often requiring high SEI values (60–1000 J/L) for satisfactory degradation. In sharp contrast, the DR-MCDBD system overcomes this bottleneck. Under optimal conditions (8-needle, 8.5 kV), it achieves robust removal (80.9% for H₂S and ~99% for organic sulfides) at an ultra-low SEI of 6.26 J/L—one to two orders of magnitude lower than the listed traditional reactors. This exceptional energy efficiency stems from the synergistic combination of the dense multi-needle discharge and the flow-deflector design, which enhances gas residence time and active species utilization, validating the system's potential for cost-effective industrial applications.

Table 1. Comparison of removal performance and energy efficiency between the DR-MCDBD reactor (under optimal conditions) and other NTP systems reported in literature.

Plasma parameters	Concentration	Energy supply	Removal efficiency	EE	By-products	Ref.
DBD	75 ppm of NH ₃	113 J/L, 19 kV	80%	/	38 ppm of O ₃ , 32 ppm of NO _x	[26]
DBD, RH=20%	20 ppm of NH ₃ and H ₂ S	2 J/L, 9 kV	95% and 54%	/	21.6 ppm of O ₃	[27]
Wire and tube plasma reactor, Q=6 L/min	80 ppm of NH ₃ and H ₂ S	235 J/L, 16 kV, 200Hz	73.3% and 84.5%	0.75 and 2g/ kWh	66.7 ppm of SO ₂ , 266.5 ppm of NO ₂ , 55.4 ppm of O ₃	[28]
Wire-mesh DBD, residence time = 1 s	4.5 ppm of H ₂ S, 6.7 ppm of CH ₃ SH and 3 ppm of NH ₃	3.37 J/L	99.8%, 100% and 100%	6.7,14.1 and 2.3 g/kWh	1.2–16 ppm of NO ₂	[29]
DBD, Q=140 L/min	125 mg/m ³ of NH ₃	78.9 J/L, 9kV	77.9%	4.5 g/kWh	0.53 mg/L of NO ₂ and 2.79 mg/L of NO ₃	[30]
Wire-plate pulse corona reactor, Q=13 m ³ /h	105 mg/m ³ of CH ₃ CH ₂ SH and 40 mg/m ³ of NH ₃	65.1 J/L, 200 Hz, 54 kV	93.1% and 100%	/	NO _x , O ₃ , SO ₂ , CO ₂ and CO	[14]
	200 mg/m ³ of CH ₃ CH ₂ SH and H ₂ S	65.1–81.4 J/L	95.6% and 100%	/	NO _x , O ₃ , SO ₂ , CO ₂ and CO	
DDBD, Q=1 L/min	100 ppm of CS ₂	960–3222 J/L, 6.52-7.04 kV	86.32% and 100%	0.35 and 1.01g/ kWh	SO ₂ and CO ₂	[15]
gliding arc discharge plasma reactor	300 mg/m ³ of NH ₃ and 200 mg/m ³ of H ₂ S	1262 J/L, 11kV	77% and 100%	0.13 g/kWh	22 mg/L of HCN and 27.8 mg/L of SO ₂	[31]
wire and tube low temperature plasma reactor	240 mg/m ³ of NH ₃ and 120 mg/m ³ of H ₂ S	202.8 J/L, 15 kV, 200 Hz	66.1% and 67.3%	/	O ₃ , SO _x and NO _x	[32]
DBD, Q=0.25 m ³ /h	22 mg/m ³ of DMDS	22.5 J/L, 20kV	61%	/	SO ₂ selectivity 33.86%	[33]

	60 mg/m ³ of DMDS	22.5 J/L, 20kV	22%	/	SO ₂ selectivity 7.75%	
	22 mg/m ³ of DMDS	10 J/L, 20kV	32.68%	/	SO ₂ selectivity 10%	
DBD, Q=3.75 L/min	75 mg/m ³ of H ₂ S	235 .2JL, 20kV	22%	0.25 g/kWh	O ₃ and SO _x	[34]
	75 mg/m ³ of H ₂ S	382.4 JL, 27.5kV	47%	0.32 g/kWh	O ₃ and SO _x	
DR-MCDBD, Q=2 m ³ /h	H ₂ S (5 ppm), CS ₂ (1.25 ppm), DMDS (2.5 ppm), CH ₃ SH (2.5 ppm), DMS (10 ppm) and NH ₃ (30 ppm)	6.26 J/L, 8.5 kV	80.9%, 45.3%, 96.2%, and 100%	1.11–16g/kWh	4.54 ppm of O ₃ , 2.06 ppm of NO _x , 1.43 ppm of SO ₂	This work

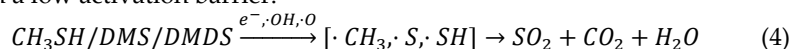
3.7. Mechanism Discussion

The experimental results above highlight a distinct disparity in removal behaviors: organic sulfides remained insensitive to flow field alterations (Figure 9b), while inorganic sulfides showed significant enhancement with the DR (Figure 9a). Based on these observations, we propose a mechanism that couples hydrodynamics with the localized energy field to interpret the degradation pathways, supported by CFD simulations and reaction kinetics analysis.

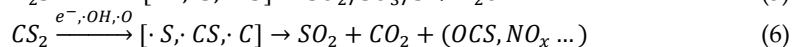
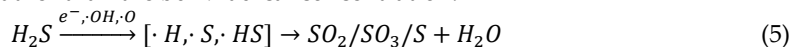
3.7.1. Molecular Intrinsic Reactivity and Degradation Pathways

The macroscopic degradation performance differs significantly between pollutants (Figure 9). This disparity fundamentally originates from differences in their Bond Dissociation Energy (BDE) and consequent reaction pathways.

Organic Sulfides (Kinetic-Controlled): As evidenced by the highly overlapping curves in Figure 9b, organic sulfides exhibited high removal efficiencies regardless of the presence of the DR. As depicted in Figure 11 (Bottom) and described in Equation (4), organic sulfides such as CH₃SH, DMS, and DMDS are characterized by relatively low BDE (e.g., C–S ≈ 2.85 eV) [35]. Their degradation proceeds via straightforward oxidation pathways initiated by bulk radicals ($\cdot\text{OH}$, $\cdot\text{O}$), rapidly yielding intermediate radicals (CH₃ \cdot , $\cdot\text{S}$) and final products (SO₂, CO₂). This constitutes a kinetically fast process with a low activation barrier.



Inorganic Sulfides (Mass Transfer-Limited): In contrast, Figure 9a reveals that the degradation of inorganic sulfides is highly dependent on the reactor configuration, with the DR yielding a marked improvement in removal efficiency. The reason lies in inorganic sulfides like CS₂ exhibit high bond dissociation energies (C=S ≈ 4.5 eV) [36]. As shown in Equations (5) and (6), the mineralization of H₂S and CS₂ is a multi-step process involving complex intermediates. Specifically, for CS₂, the dissociation of the strong C=S bond and the subsequent oxidation of intermediates (e.g., OCS, Carbonyl Sulfide) necessitate high-energy electron impacts (e^-), rendering the process highly sensitive to the local energy density rather than the bulk radical concentration.



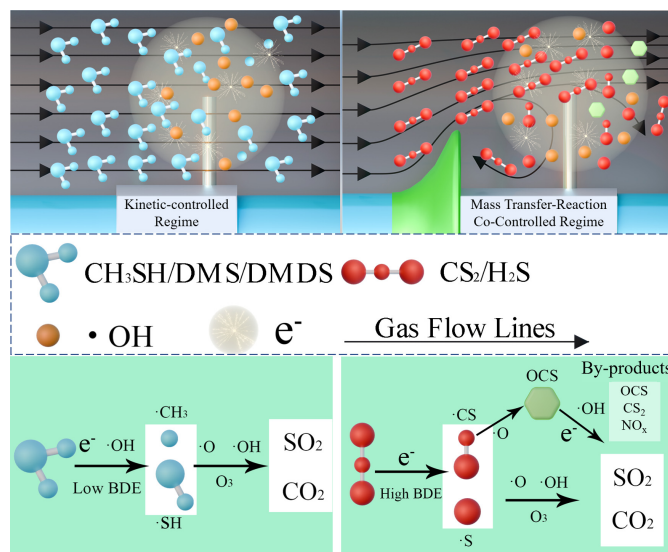


Figure 11. Schematic of the synergistic degradation mechanism in the DR-MCDBD reactor. (Top) Conceptual flow regimes: kinetic-controlled (left) and mass transfer-reaction co-controlled (right, enabled by the deflector ring). (Bottom) Proposed reaction pathways for organic sulfides (left) and inorganic sulfides (right).

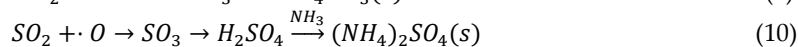
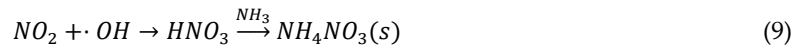
3.7.2. Chemical Synergy and Terminal Aerosol Formation

Beyond the independent degradation pathways, a distinct synergistic effect exists between NH_3 and sulfur-containing compounds, which significantly enhances the overall removal efficiency [37].

Radical Propagation: The co-existence of NH_3 and H_2S establishes a self-sustaining radical cycle. The reactive hydrogen atoms ($\cdot\text{H}$) released from H_2S dissociation (Equation (5)) act as cross-initiators. Concurrently, bulk radicals ($\cdot\text{OH}$, $\cdot\text{O}$) accelerate the decomposition of NH_3 into amino radicals ($\cdot\text{NH}_2$) via hydrogen abstraction, as shown in Equation (7). Note that the reaction with $\cdot\text{O}$ generates secondary $\cdot\text{OH}$ radicals, further propagating the chain reaction. The generated NH_2 subsequently contributes to De- NO_x processes (Equation (8)).



Gas-to-Particle Conversion (Terminal Removal): A critical removal mechanism is the in-situ conversion of gaseous pollutants into solid aerosols. As depicted in Equations (9) and (10), the acidic oxidation products (HNO_3 and H_2SO_4) are proposed to react with excess NH_3 to form ammonium nitrate and ammonium sulfate.



This mechanism is substantiated by the experimental observation of yellowish-white solid residues accumulating on the inner surface of the dielectric barrier tube. The white precipitates are consistent with the formation of ammonium salts, whereas the yellowish traces suggest the co-deposition of elemental sulfur derived from H_2S dissociation (Equation (5)). These solid by-products confirm that a portion of the pollutants is removed via phase transition rather than mere gaseous oxidation.

3.7.3. Spatial Mismatch and Flow Field Reconstruction

In the baseline MCDBD configuration without the DR, the CFD velocity profiles presented in Figure 8a reveal a critical "Bypass Effect." A significant fraction of the gas stream flows through the interstitial spaces, effectively bypassing the active high-energy zones at the needle tips. This confirms the spatial mismatch where the bulk gas velocity is decoupled from the discharge energy density.

The introduction of the DR functions as a passive process intensification strategy. As shown in the flow topology in Figure 8b, the DR mechanically blocks the low-field zones and forces the gas stream to converge toward the high-energy electron avalanche zone (indicated by the high-velocity regions). Furthermore, the recirculation vortices observed downstream of the DR structure (refer to Figure 8b) extend the residence time of pollutants. This hydrodynamic reconstruction ensures that intermediates (like OCS) and precursors for salt formation remain within the radical-rich environment long enough to undergo complete conversion.

3.7.4. Unified Synergistic Mechanism

Based on the distinct responses to flow field modulation (refer to Figure 8), the degradation process can be categorized into two distinct regimes, as visualized in the upper panel of Figure 11:

1. Kinetic-Controlled Regime (Organic Sulfides);

For organic sulfides possessing low BDE, the overall reaction rate is primarily governed by intrinsic chemical kinetics rather than physical transport. As shown in the left panel of Figure 11, these highly reactive molecules can be effectively degraded by radicals dispersed in the bulk flow. This explains the negligible enhancement provided by the DR as observed in Figure 9b.

2. Mass Transfer-Reaction Co-Controlled Regime (Inorganic Sulfides).

For refractory molecules like CS₂ (High BDE), degradation is strictly confined to the high-energy streamer channels. The DR establishes a co-controlled regime (right panel of Figure 11): it enhances mass transfer by directing pollutants into the discharge zone and promotes reaction completeness by extending residence time. This mechanism perfectly elucidates the experimental results in Figure 9a, where inorganic sulfide removal rose sharply with flow optimization.

4. Conclusions

This study developed a novel Dielectric Barrier Discharge reactor (DR-MCDBD) to resolve the conflict between gas throughput and energy efficiency. The reactor features a Multi-Needle to Cylinder configuration integrated with Flow Deflector Rings. Optimization tests identified the 8-needle topology as the ideal geometry, as it effectively balances discharge density with electric field shielding. Furthermore, the Flow Deflector Rings successfully reconstructed the hydrodynamic field. By mitigating the “bypass effect” and inducing local turbulence, this modification extended gas residence time and enhanced collision probabilities.

Crucially, the study elucidated distinct degradation behaviors. Organic sulfide removal was primarily kinetically controlled. In contrast, refractory inorganic sulfides (e.g., CS₂) followed a mass transfer-reaction co-controlled mechanism. This distinction highlights the necessity of hydrodynamic modulation to overcome mass-transfer limitations. Under optimal conditions, the system removed over 80% of H₂S and nearly 100% of organic sulfides. Notably, these results were achieved at a remarkably low Specific Energy Input of 6.26 J/L, with negligible NO_x production. Ultimately, the synergistic regulation of discharge and flow fields establishes the DR-MCDBD reactor as a scalable, high-efficiency solution for industrial odor control.

Author Contributions: Q.Q., J.Z. and Y.Z. developed the idea of this study; Q.Q., J.Z. and Q.X. conducted the calculations and experiments; data analysis was performed by Q.Q. and Y.Z.; H.L. and N.H. revised the manuscript. All authors have read and agreed to the published version of the manuscript.

Funding: This work was supported by the National Key R&D Program of China under Zhejiang University Funding Project (DZL202517).

Data Availability Statement: Data are contained within the article.

Conflicts of Interest: The authors declare no conflicts of interest.

References

1. Y. Wang, M. Han, T. Jia, X. Hu, H. Zhu, Z. Tong, Y. Lin, C. Wang, D. Liu, Y. Peng, G. Wang, J. Meng, Z. Zhai, Y. Zhang, J. Deng, H. Hsi, Emissions, measurement, and control of odor in livestock farms: a review, *Sci. Total Environ.* **2021**, vol.776, 145735.
2. R. Tong, L. Zhang, X. Yang, J. Liu, P. Zhou, J. Li, Emission characteristics and probabilistic health risk of volatile organic compounds from solvents in wooden furniture manufacturing, *J. Clean. Prod.* **2019**, vol.208, 1096–1108.
3. M.K. Nguyen, C. Lin, H.G. Hoang, X.T. Bui, H.H. Ngo, V.G. Le, H. Tran, Investigation of biochar amendments on odor reduction and their characteristics during food waste co-composting, *Sci. Total Environ.* **2023**, vol.865, 161128.
4. X. Wang, A. Selvam, S.S.S. Lau, J.W.C. Wong, Influence of lime and struvite on microbial community succession and odour emission during food waste composting, *Bioresour. Technol.* **2018**, vol.247, 652–659.
5. M. Schiavon, L.M. Martini, C. Corra, M. Scapinello, G. Coller, P. Tosi, M. Ragazzi, Characterisation of volatile organic compounds (VOCs) released by the composting of different waste matrices, *Environ. Pollut.* **2017**, vol.231, 845–853.
6. X. Chen, Y. Geng, T. Fujita, An overview of municipal solid waste management in China, *Waste Manag.* **2010**, vol.30, 716–724.
7. B. Scaglia, V. Orzi, A. Artola, X. Font, E. Davoli, A. Sanchez, F. Adani, Odours and volatile organic compounds emitted from municipal solid waste at different stage of decomposition and relationship with biological stability, *Bioresour. Technol.* **2011**, vol.102, 4638–4645.
8. C.A. Rincón, A. De Guardia, A. Couvert, D. Wolbert, S. Le Roux, I. Soutrel, G. Nunes, Odor concentration (OC) prediction based on odor activity values (OAVs) during composting of solid wastes and digestates, *Atmos. Environ.* **2019**, vol.201, 1–12.
9. H. Wu, H. Yan, Y. Quan, H. Zhao, N. Jiang, C. Yin, Recent progress and perspectives in biotrickling filters for VOCs and odorous gases treatment, *J. Environ. Manag.* **2018**, vol.222, 409–419.
10. M.J. Jafari, A.H. Matin, A. Rahmati, M.R. Azari, L. Omid, S.S. Hosseini, D. Panahi, Experimental optimization of a spray tower for ammonia removal, *Atmos. Pollut. Res.* **2018**, vol.9, 783–790.
11. C.W. Park, J.H. Byeon, K.Y. Yoon, J.H. Park, J. Hwang, Simultaneous removal of odors, airborne particles, and bioaerosols in a municipal composting facility by dielectric barrier discharge, *Sep. Purif. Technol.* **2011**, vol.77, 87–93.
12. Z. Zheng, X. Zhang, K. Li, H. Pi, B. Du, C. Li, X. Shi, Y. Hu, Y. Jin, Z. Zhu, M. Yuan, H. Lu, X. Chen, Simultaneous treatment of various malodorous substances in gas by non-thermal plasma, *IEEE Trans. Plasma Sci.* **2023**, vol.51(2), 414–420.
13. H. Kim, A.A. Abdelaziz, Y. Teramoto, T. Nozaki, K. Hensel, Y. Mok, S. Saud, Duc Ba Nguyen, D.H. Lee, W.S. Kang, Interim report of plasma catalysis: footprints in the past and blueprints for the future, *Int. J. Plasma Environ. Sci. Technol.* **2021**, vol.15, e01004.
14. Y. Shi, J. Ruan, X. Wang, W. Li, T. Tan, Decomposition of mixed malodorants in a wire-plate pulse corona reactor, *Environ. Sci. Technol.* **2005**, vol.39, 6786–6791.
15. Muhammad Farooq Mustafa, Xindi Fu, Yanjun Liu, Yawar Abbas, Hongtao Wang, Wenjing Lu, Volatile organic compounds (VOCs) removal in non-thermal plasma double dielectric barrier discharge reactor, *Journal of Hazardous Materials* **2018**, vol.347, 317–324.
16. S. Jiang, K. Guo, Y. Wang, Z. Li, J. Rao, Research on discharge characteristics of three-electrode load under the pulsed power supply, *IEEE Trans. Plasma Sci.* **2022**, vol.50(5), 1255–1261.
17. X. Wang, Q. Yang, C. Yao, X. Zhang, C. Sun, Dielectric barrier discharge characteristics of multineedle-to-cylinder configuration, *Energies* **2011**, vol.4, 2133–2150.
18. Alexander Bötdecker et al., The role of flow field dynamics in enhancing volatile organic compound conversion in a surface dielectric barrier discharge system, *J. Phys. D: Appl. Phys.* **2024**, vol.58, 025208.
19. X. Wei, Z. Tao, J. Xinrui, X. Huan, Degradation of mixed typical odour gases via non-thermal plasma catalysis, *J. Hazard. Mater.* **2022**, vol.440, 129751.
20. X. Zeng, B. Li, R. Liu, X. Li, T. Zhu, Investigation of promotion effect of Cu doped MnO₂ catalysts on ketone-type VOCs degradation in a one-stage plasma-catalysis system, *Chem. Eng. J.* **2020**, vol.384, 123362.

21. Y. Inomata, K. Matsunaga, Y. Murai, K. Osada, Y. Iwasaka, Simultaneous measurement of volatile sulfur compounds using ascorbic acid for oxidant removal and gas chromatography–ffame photometric detection, *J. Chromatogr. A.* 1999, vol.864, 111–119.
22. M. Wi’sniewska, A. Kulig, K. Lelicin’ska-Seraffn, The impact of technological processes on odorant emissions at municipal waste biogas plants, *Sustainability* 2020, vol.12, 5457.
23. N. Masey, J. Gillespie, E. Ezani, C. Lin, H. Wu, N.S. Ferguson, S. Hamilton, M. R. Heal, I.J. Beverland, Temporal changes in field calibration relationships for Aeroqual S500 O3 and NO2 sensor-based monitors, *Sens. Actuators B Chem.* 2018, vol.273, 1800–1806.
24. Z. Deng, Q. Qiu, H. Jia, W. Zhu, Y. Deng and X. He, Load Characteristic Analysis of Dielectric Barrier Discharge With Multineedle to Coaxial Cylindrical Configuration, *IEEE Transactions on Plasma Science* 2025, vol. 53(4), 661-668.
25. T. C. Manley, The electric characteristics of the ozonator discharge, *Trans. Electrochem. Soc.* 1943, vol. 84(1), 83–96.
26. C.W. Park, J.H. Byeon, K.Y. Yoon, J.H. Park, J. Hwang, Simultaneous removal of odors, airborne particles, and bioaerosols in a municipal composting facility by dielectric barrier discharge, *Sep. Purif. Technol.* 2011, vol.77, 87–93.
27. Z. Zheng, X. Zhang, K. Li, H. Pi, B. Du, C. Li, X. Shi, Y. Hu, Y. Jin, Z. Zhu, M. Yuan, H. Lu, X. Chen, Simultaneous treatment of various malodorous substances in gas by non-thermal plasma, *IEEE Trans. Plasma Sci.* 2023, vol.51(2), 414–420.
28. W. Liang, L. Ma, J. Li, J. Li, F. Zheng, Control of hydrogen sulfide by a wire-tube dielectric barrier discharge AC plasma reactor, *Clean. -Soil Air Water* 2012, vol.40(6), 586–591.
29. G.W. Yang, S.M. Chun, K.I. Kim, H.J. Lee, Y. Hong, Simulated experiments for removal of odorous gases by wire-mesh electrode dielectric barrier discharge, *Phys. Plasmas* 2022, vol.29, 093502.
30. L. Xia, L. Huang, X. Shu, R. Zhang, W. Dong, H. Hou, Removal of ammonia from gas streams with dielectric barrier discharge plasmas, *J. Hazard. Mater.* 20228, vol.152, 113–119.
31. Shengyong Lu, Lu Chen, Qunxing Huang, Liqin Yang, Changming Du, Xiaodong Li, Jianhua Yan, Decomposition of ammonia and hydrogen sulfide in simulated sludge drying waste gas by a novel non-thermal plasma, *Chemosphere* 2014, vol.117, 781-785.
32. Xie Wei, Zhu Tao, Jin Xinrui, Xu Huan, Degradation of mixed typical odour gases via non-thermal plasma catalysis, *Journal of Hazardous Materials* 2022, vol.440, 129751.
33. Nacer Belkessa, Amine Aymen Assadi, Phuong Nguyen Tri, Abdelkrim Bouzaza, Non-thermal plasma/ photocatalysis processes for dimethyl disulfide removal: Study and reduction of the catalyst poisoning, *Catalysis Today* 2025, vol.458, 115380.
34. Jie Chen, Zhenmiao Xie, Removal of H2S in a novel dielectric barrier discharge reactor with photocatalytic electrode and activated carbon fiber, *Journal of Hazardous Materials* 2013, vol.261, 38-43
35. Y. Shi, J. Ruan, X. Wang, W. Li, T. Tan, Decomposition of mixed malodorants in a wire-plate pulse corona reactor, *Environ. Sci. Technol.* 2005, vol.39, 6786–6791.
36. C. Tsai, W. Lee, C. Chen, W. Liao, Decomposition of CH3SH in a RF plasma reactor: reaction products and mechanisms, *Ind. Eng. Chem. Res.* 2001, vol.40, 2384–2395
37. Z. Zheng, X. Zhang, K. Li, H. Pi, B. Du, C. Li, X. Shi, Y. Hu, Y. Jin, Z. Zhu, M. Yuan, H. Lu, X. Chen, Simultaneous treatment of various malodorous substances in gas by non-thermal plasma, *IEEE Trans. Plasma Sci.* 2023, vol.51(2), 414–420.

Disclaimer/Publisher’s Note: The statements, opinions and data contained in all publications are solely those of the individual author(s) and contributor(s) and not of MDPI and/or the editor(s). MDPI and/or the editor(s) disclaim responsibility for any injury to people or property resulting from any ideas, methods, instructions or products referred to in the content.